Here, we discuss methods for addressing bubble growth. Covered are the equation of state, experimental heating, and Raman approaches.

A1.1. Equation of state reconstruction

Here we describe the observed volume and two different calculated volume approaches to equation of state CO_2 reconstructions, which are all included in the MIMiC (Melt Inclusion Modification Correction) program (Appendix 2). In these methods, the mass of CO_2 in the vapor bubble is calculated using an equation of state, and that CO_2 is added into the glass composition by mass balance. We use the Redlich-Kwong equation of state (Eq. A1.1) to calculate the molar volume of CO_2 ($\bar{V}_{CO2}$) in the vapor bubble.

$$P = \frac{R \cdot T}{\bar{V}_{CO2} - b} - \frac{a}{\sqrt{T} \cdot \bar{V}_{CO2} \cdot (\bar{V}_{CO2} + b)} \qquad \textbf{(A1.1)}$$

R is the gas constant (8.314 $J \cdot K^{-1} \cdot mol^{-1}$). The observed and calculated volume methods use different temperatures (T), which are described below. Pressure (P) is set to the vapor saturation pressure that is calculated using the volatile contents of the glass. Two parameters address the non-ideality of gas: a is a constant correcting for attractive potential between molecules and b is a constant correcting for the volume of gas molecules. They are calculated using Eqs. A1.2 and A1.3 with data on the temperature (T_c) and pressure (P_c) at the critical point of the gas.

$$a = 0.4275 \cdot \frac{R^2 \cdot T_c^{2.5}}{P_c} \qquad \textbf{(A1.2)}$$

$$b = 0.08664 \cdot \frac{R \cdot T_c}{P_c} \qquad \textbf{(A1.3)}$$

We take values of T_c (304.1282 K) and P_c (73.773$\cdot 10^5$ Pa) from Duan and Zhang (2006). The molar volume of CO_2 ($\bar{V}_{CO2}$) is determined by finding the root of Eq. A1.1. With $\bar{V}_{CO2}$, we calculate the mass of CO_2 (M_{CO2}) in the vapor bubble using the following equation with a molecular mass of CO_2 (MM_{CO2}) of 44.01 $g \cdot mol^{-1}$.

$$M_{CO2} = \frac{V_{VB} \cdot X_{CO2} \cdot MM_{CO2}}{\bar{V}_{CO2}} \qquad \textbf{(A1.4)}$$

As the names imply, the vapor bubble volume (V_{VB}) is observed for the observed volume approach and calculated for the calculated volume approach. The mole fraction of CO_2 in the vapor phase (X_{CO2}) is calculated using the volatile contents of the glass with VolatileCalc (Newman and Lowenstern, 2002). We note that in place of the Redlich-Kwong equation of state, some studies have used the ideal gas law (e.g., Shaw et al., 2010; Hauri et al., 2018).

A1.1.1. Observed volume approach

In the observed volume approach, equilibrium between the vapor bubble and melt at the time of quench is assumed. Therefore, the observed volume of the vapor bubble (V_{VB}) is used to calculate the mass of CO_2 (M_{CO2}) in the vapor bubble (Eq. A1.4). For the equation of state calculation (Eq. A1.1), the temperature (T) is set to the glass transition temperature (T_g). T_g is calculated using the formulation of Zhang et al. (2007), in which T_g is calculated based on cooling rate (q) and a viscosity (η_g) threshold. For q, we use values approach for the clast size of each sample: 20 °C/s for ash, 10 °C/s for lapilli and bomb rims, and 1 °C/s for bomb interiors. Except for ash, these are conductive cooling rates calculated by Lloyd et al. (2013). The cooling rate for ash comes from experiments by Xu and Zhang (2002).

$$\eta_g = \frac{10^{11.45}}{q} \qquad \textbf{(A1.5)}$$

In order to calculate T_g from Eq. A1.5, we perform an iterative viscosity calculation varying T until η_g is reached. We use the viscosity model of Giordano et al. (2008) with the measured composition of the melt inclusion.

The approach we describe is similar to approaches used by other studies (e.g., Shaw et al., 2010; Wanless et al., 2014; Colman et al., 2015; Hauri et al., 2018). One key difference is that, for each individual melt inclusion, we calculate T_g. Previous studies have used a single value of T_g for an entire suite of melt inclusions.

Method

Observations of melt inclusion and bubble volumes

Prior to melt inclusion intersection, melt inclusion and vapor bubble volumes must be determined. This is usually done petrographically, assuming the bubble is a sphere and the melt inclusion an ellipsoid. Several measurements of the diameter of the bubble (visible in the 2-D) are averaged and used to calculate volume. Two dimensions of the sectioned melt inclusion are measured directly, and the third dimension (not visible petrographically) is typically assumed to be equivalent to the short-measured dimension (e.g., Aster et al., 2016; Rasmussen et al., 2018). The basis for this assumption is that a common strategy for mounting melt inclusions is to put the shortest dimension normal to the cross-sectional plane in order to maximize the exposed surface area of the melt inclusion. Alternatively, the thickness of the melt inclusion can be measured by focusing to the top and bottom of the inclusion using a calibrated stage. In practice, this is inexact because many melt inclusions have smooth interfaces that don't come into sharp focus. The best way to measure volumes of the vapor bubble and melt inclusion is using a 3-D imaging technique, such as x-ray tomography (e.g., Pamukcu et al., 2015). Following volume observations, the melt inclusion is analyzed for major element and volatile contents.

Equation of state calculation

The Redlich-Kwong equation of state (Eq. A1.1) is used to calculate the mass of CO_2 in the vapor bubble.

Reconstruction of CO_2

The restored CO_2 content is determined by performing a mass balance calculation (Eq. A1.6). The density of the melt inclusion is determined using the measured composition and partial molar volumes (e.g., Lesher and Spera, 2015) of each chemical component . The mass of the melt inclusion is calculated using the density (ρ_{MI}) and volume (V_{MI}) of the melt inclusion. It should be noted that the vapor bubble volume percent can be used in lieu of individual measurements of the vapor bubble (Eq. A1.4) and melt inclusion volumes (Eq. A1.6). The MIMiC program (Appendix 2) uses the vapor bubble volume percent to perform this calculation.

$$CO_{2\ restored} = CO_{2\ glass} + \frac{M_{CO2}}{V_{MI} \cdot \rho_{MI}} \qquad (\mathbf{A1.6})$$

A1.1.2. Calculated volume approach

Unlike the observed volume approach, the calculated volume approach does not assume vapor-melt equilibrium during quench. Rather, CO_2 diffusion into the vapor bubble is considered to be rate-limited by the diffusivity of CO_2 (as CO_3^{2-} in basalts) in melt. This means that during rapid cooling, there is a phase of vapor bubble expansion, driven by thermal contraction of the melt, without significant diffusive addition of CO_2 into the vapor bubble. For melt inclusions with any but the lowest cooling rates, this is likely the case (see Fig. 7 in the main text and related discussion). The implication is that the observed bubble volume is not in vapor-melt equilibrium and a calculated bubble volume must be used in the CO_2 reconstruction.

We describe two different calculated volume approaches: the Riker (2005) model and our new vapor bubble growth model. Other models exist (e.g., Steele-Macinnis et al., 2011; Sides et al., 2014; Maclennan, 2017), but they are not openly available. The models calculate bubble volume using different approaches, but they are based on similar principles. Each considers three states of a melt inclusion with associated intensive (e.g., pressure, temperature, density) and extensive (e.g., mass, volume) proprieties. The *initial* state describes the conditions of melt inclusion at the time of entrapment, which may be reflected in the composition of a melt inclusion that has been corrected for post-entrapment processes (post-entrapment crystallization/melting - PEC/PEM, diffusive water-loss, vapor bubble growth). The models differ in how the *intermediate* state is viewed. In the Riker (2005) model, and also the model of Aster et al. (2016) that builds on it, the *intermediate* state describes the melt inclusion immediately prior to ascent and eruption. Post-entrapment modifications are assumed to have completed at that time without kinetic limitations. Ascent, eruption, and quench are assumed to be rapid enough such that the composition of the melt inclusion is not significantly affected. In our vapor bubble growth model, the *intermediate* state is considered to occur when CO_2 ceases entering the bubble in appreciable quantities. We consider this state to occur at the closure temperature for CO_2 (see the *Discussion* section of the main text). With our approach, no assumption about when post-entrapment processes occurred is required. This is an improvement over the model of Riker (2005) because, in many cases, post-entrapment processes occur during quench (see the *Discussion* section of the main text). In both models, the bubble volume used for the equation of state correction is the calculated *intermediate* state bubble volume. The *final* state describes the conditions of the melt inclusion upon quench. The *final* composition is the measured composition. The *intermediate* composition is identical, except for chemical components that are affected by cooling and close at a lower temperature than CO_2. The physical conditions (e.g., pressure, temperature) of the *intermediate*

and *final* states are significantly different. To determine bubble volume, the methods consider the volume of the melt inclusion in the *intermediate* and *initial* states. If the volume of the *initial* melt inclusion is found to be greater than the *intermediate* melt inclusion, a vapor bubble is assumed to take up the excess volume.

In both models, the melt inclusion system is comprised of similar components. In our model, the *initial* melt inclusion contains melt, possibly a vapor bubble, and, if PEM occurred, the volume of olivine that melted. The Riker (2005) model has a similar initial state, except heating and PEM are not considered by the model. So, the volume of olivine that melted if PEM occurred is not considered. In both models, the *intermediate* melt inclusion includes melt, possibly a vapor bubble, and, if PEC occurred, the volume of olivine that crystallized.

A1.1.2.1. Riker (2005) vapor bubble growth model

Riker (2005) developed an approach for reconstructing the entrapped CO_2 contents of melt inclusions, which is based on the approach of Anderson and Brown (1993). The model was described by Wallace et al. (2015) and improved, but tailored for a specific application, by Aster et al. (2016). In the model, bubble growth results from cooling (from the *initial* to the *intermediate* state), causing thermal contraction of the melt inclusion (the host is assumed to have a negligible thermal expansivity) and crystallization of olivine. Volume change associated with thermal contraction is based on calculations using partial molar volumes of Lange (1997) and the average composition of melt inclusions from Mauna Loa. Volume change associated with olivine crystallization is calculated by determining the extent of olivine crystallization for a given amount of cooling, which is based on an assumed linear relationship (Montierth et al., 1995), and taking difference in density between the olivine (assumed to be 3.34 g/cm^3) and melt inclusion (assumed to be 2.68 g/cm^3). Taking the cooling from the *initial* temperature (T_i) to the *intermediate* temperature (T_{int}), the model predicts the volume percent of the vapor bubble (Eq. A1.7).

$$VB\ (vol\%) = 0.0162 \cdot (T_i - T_{int}) \qquad (\textbf{A1.7})$$

Method

Initial temperature (T_i)
   The melt inclusion is corrected for PEC/PEM (and diffusive Fe-Mg exchange, if necessary). The Riker (2005) model does not explicitly address diffusive loss of H^+. So, a water-loss correction is not applied. T_i is calculated using the corrected melt inclusion and the measured host compositions. We use the olivine-melt thermometer (eqn. 4) of Putirka et al. (2007).

Intermediate temperature (T_{int})
   T_{int} is calculated with the olivine-melt thermometer used to calculate T_i. In this case, calculated equilibrium olivine and measured melt inclusion compositions are used. The equilibrium olivine is determined by calculating a distribution coefficient that describes partitioning of Fe and Mg between the host and the melt inclusion ($K_D^{Fe\text{-}Mg}$) and applying $K_D^{Fe\text{-}Mg}$ to the measured melt inclusion composition. We calculate $K_D^{Fe\text{-}Mg}$ using the model of Toplis (2005).

Equation of state calculation

The Redlich-Kwong equation of state (Eq. A1.1) is used to calculate the molar volume of CO_2 in the vapor bubble ($\bar{V}_{CO2}$). The temperature is set to T_{int}. The mass of CO_2 (M_{CO2}) is calculated using Eq. A1.4. The model provides the volume percent of the vapor bubble (V_{VB}). Therefore, the value used for this calculation is arbitrary, provided the volume of the melt inclusion (for mass balance, next step) is consistent with the modeled vapor bubble.

Mass balance calculation
The restored CO_2 content ($CO_{2\ restored}$) is determined using Eq. A1.6.

A1.1.2.2. Our vapor bubble growth model

Here we describe the vapor bubble growth model that we developed for MIMiC. Volume difference between the *initial* and *intermediate* state melt inclusions arises from several processes.

Host deformation. Temperature change causes thermal contraction or expansion of the host, and changes in the external pressure cause elastic and plastic deformation of the host. These processes lead to a change in the volume of the melt inclusion cavity. Additionally, plastic deformation of the host can occur, but our model does not account for this process (Schiavi et al., 2016).
Temperature change. The change in temperature from the *initial* (i.e., entrapment) temperature and the CO_2 closure temperature results in a volume change of the melt and host due to thermal expansivity.
Pressure change. The volume of the melt inclusion is set by the void space in the host olivine. Therefore, the processes that cause volume changes are accommodated by changes in pressure and possibly, in the case of a decrease in volume, growth of a vapor bubble. A change in pressure will be reflected in a change in the partial molar volumes of each melt component.
Olivine crystallization/melting. Creates a volume difference in the melt inclusion if the molar volumes of olivine and melt are different (in general, olivine has a smaller molar volume). This also has the effect of changing the volume of the melt because composition (hence, density) and mass change as olivine crystallizes.
Diffusive gain/loss of Fe by diffusive exchange of Fe-Mg. Causes a change in volume of the melt because FeO and MgO have different partial molar volumes.
Loss of CO_2. CO_2 may be lost to a vapor bubble, which decreases the mass of the melt, leading to a decrease in melt volume.

Our model builds on the earlier model of Riker (2005) in several ways, including incorporation of pressure in molar volume calculations and accounting for elastic and thermal host deformation.

To determine the volume of the vapor bubble, we must assess the volume of the melt inclusion in the *initial* and *intermediate* states. If the *intermediate* volume is calculated to be less than the *initial* volume, bubble growth is predicted. In this case, the *initial* volume is recalculated using an iterative method because there are several positive and negative feedbacks affecting bubble growth (i.e., a greater extent of bubble growth implies a higher trapping pressure, which in turn leads to a smaller calculated *initial* volume due to the effect of pressure on the partial molar volumes of the melt components and reduces the calculated bubble volume). It should be noted that the calculations are performed by arbitrarily setting the initial melt mass to 100 g. We track

the change in mass from the *initial* to the *intermediate* state by calculating the mass fraction of olivine crystallized (or melted) over this interval and adjusting the mass accordingly.

First initial volume calculation

Step 1. Determine partial molar volumes.
Partial molar volumes for each melt component are determined using those compiled by Lesher and Spera (2015), which are from Lange and Carmichael (1987) and Ochs and Lange (1999). Most partial molar volumes are dependent on temperature and pressure.
- Temperature is set to the *initial* temperature (T_i), which is calculated using eqn. 4 of Putirka et al. (2007). This calculation involves several parameters.
  - *Melt composition*: Set to the PEC/PEM-corrected composition.
  - *Olivine composition*: Set to the measured host composition (Fo_{host}).
  - *Pressure*: Set to the *initial* pressure (P_i, see below).
- Pressure is set to the *initial* pressure (P_i), which is calculated with Newman and Lowenstern (2002). This calculation involves several parameters.
  - Melt H_2O contents: Set to the PEC/PEM-corrected contents.
  - Melt CO_2 contents: Set to the PEC/PEM-corrected contents.
  - Melt SiO_2 contents: Set to the PEC/PEM-corrected contents. If SiO_2 content is >49 wt.% or <40 wt% (i.e., outside of the compositional range of the model), we set the values to 49 wt% and 40 wt% (respectively).
  - Temperature: Set to T_i.
- ***Note:*** In the iterative initial volume calculation below, we recalculate values for T_i and P_i using the bubble growth corrected parameters.

Step 2. Calculate volume.
The initial volume ($V_{i,melt}$) of the melt is calculated using the PEC/PEM corrected melt inclusion composition. The melt inclusion mass is set to 100 g.
- The volume is calculated in two steps.
  - The moles of each melt component (Nj) is calculated by dividing mass (Mj) by molecular mass (MMj).

$$Nj = \frac{Mj}{MMj} \qquad (\textbf{A1.8})$$

  - The *initial* volume ($V_{i,melt}$) of the melt is calculated by multiplying the moles of each melt component (Nj) by each of their partial molar volumes ($\overline{V}j$) and adding these numbers together.

$$V_{i,melt} = \sum Nj \cdot \overline{V}j \qquad (\textbf{A1.9})$$

Step 3. Recalculate melt inclusion volume.
The volume of the melt inclusion is calculated based on whether PEC/PEM occurred.
- If PEC occurred, the volume of the initial melt inclusion (V_i) is the volume calculated in Eq. A1.9.

- If PEM occurred, we add the volume of olivine that melted to the initial volume (Eq. A1.10). The mass of PEM olivine (M_{olv}) is the wt% of PEM olivine calculated in the PEC/PEM correction (Appendix 2).

$$V_i = V_{i,melt} + \frac{M_{olv}}{\rho_{olv}} \qquad (\mathbf{A1.10})$$

- The density of the olivine (ρ_{olv}) is calculated in several steps. The olivine of interest has an Fo intermediate between the host olivine Fo (Fo_{host}) and the olivine Fo in equilibrium with the *intermediate* state melt inclusion (Fo_{int}). The molar volume of the olivine of interest at standard temperature and pressure ($\bar{V}_{olv,0}$) is calculated by assuming a linear relationship between Fo and volume (Eq. A1.11). Molar volumes are calculated using densities for forsterite (3.222 g/cm³) and fayalite (4.400 g/cm³) from Hacker et al. (2003) and molar masses for forsterite and fayalite ($MM_{forsterite}$ and $MM_{fayalite}$, respectively).

$$\bar{V}_{olv,0} = \frac{MM_{forsterite}}{\rho_{forsterite}} + \left(\frac{MM_{fayalite}}{\rho_{fayalite}} - \frac{MM_{forsterite}}{\rho_{forsterite}} \right) \cdot \left(1 - \frac{Fo_{host} + Fo_{int}}{100} \right) \qquad (\mathbf{A1.11})$$

- The molar volume of olivine at P_i and T_i ($\bar{V}_{olv,PT}$) is calculated using the high-temperature Birch-Murnaghan equation of state, as described by Liu and Li (2006). We take values of the isothermal bulk modulus ($K_{0,T}$), 129.0 GPa, and its pressure derivative ($K'_{0,T}$), 4.61, from Liu et al. (2005a), which are for San Carlos olivine.

$$P_i = \frac{3}{2} K_{0,T} \cdot \left(\left(\frac{\bar{V}_{olv,0T}}{\bar{V}_{olv,PT}} \right)^{\frac{7}{3}} - \left(\frac{\bar{V}_{olv,0T}}{\bar{V}_{olv,PT}} \right)^{\frac{5}{3}} \right) \cdot \left(1 + \frac{3}{4} \cdot (K'_{0,T} - 4) \cdot \left(\left(\frac{\bar{V}_{olv,0T}}{\bar{V}_{olv,PT}} \right)^{\frac{2}{3}} - 1 \right) \right) \qquad (\mathbf{A1.12})$$

- Olivine molar volume at T_i and standard pressure ($\bar{V}_{olv,0T}$) is described by the following equation (A1.13). Values for α_0 (2.73E-5 K⁻¹), α_1 (2.22E-8 K⁻¹), and α_2 (not fit, assumed to be negligible) are from Liu and Li (2006), which are for San Carlos olivine.

$$\bar{V}_{olv,0T} = \bar{V}_{olv,0} \cdot exp \int_{298.15}^{T_i + 273.15} \alpha_0 + \alpha_1 T + \alpha_2 T^{-2} dT \qquad (\mathbf{A1.13})$$

- We calculate ρ_{olv} with the following equation (A1.14) and the molar mass of the olivine of interest (MM_{olv}).

$$\rho_{olv} = \frac{MM_{olv}}{\bar{V}_{olv,PT}} \qquad (\mathbf{A1.14})$$

- To account for the effect of elastic deformation and cooling on the volume of the melt inclusion, we use equation 18 in Zhang (1998), which describes elastic equilibrium in an inclusion-host system. In the following equation (A1.15), the fractional volume change of the melt inclusion $\left(\frac{\Delta V_i}{V_{i0}} \right)$ is calculated.

$$\frac{\Delta V_i}{V_{i0}} \approx \frac{P_0 - P_{out}}{K_h} + \gamma_h + \left(\frac{P_{in} - P_{out}}{1 - \frac{R_i^3}{R_h^3}}\right) \cdot \left(\frac{\frac{R_i^3}{R_h^3}}{K_h} + \frac{3}{4G_h}\right) \qquad (\mathbf{A1.15})$$

- o The parameters are as follows (all of the pressure terms are in GPa).
  - ▪ Initial pressure (P_0): Set to P_i (initially calculated in step 1, and later calculated iteratively).
  - ▪ Pressure of the exterior environment during the intermediate state (P_{out}): Set to atmospheric pressure (0.1 MPa).
    - The basis for using atmospheric pressure for the pressure of the intermediate state is that the intermediate state is thought to occur during quench, which, for subaerial eruptions, occurs at atmospheric pressure.
  - ▪ Internal pressure (P_{in}): Set to the pressure of the melt inclusion in the *intermediate* state (P_{int}), see step 2 of the *intermediate* volume calculation.
  - ▪ Bulk modulus (K_h): Set to 129.0 GPa (Liu et al., 2005b).
  - ▪ Shear modulus (G_h): Set to values for San Carlos olivine (Abramson et al., 1997). For simplicity, *P* is set to P_{out} (in GPa).

$$G_h = 78 + 1.71 \cdot P - 0.027 \cdot P^2 \qquad (\mathbf{A1.16})$$

  - ▪ Temperature effect on elastic constants (γ_h): Calculated with the following equation (A1.17). T_{CO2} is the closure temperature for CO_2 (i.e., the *intermediate* temperature). The thermal parameters are the same used in A1.13.

$$\gamma = \int_{298.15}^{T_{CO2}+273.15} \alpha_0 + \alpha_1 T + \alpha_2 T^{-2} dT \qquad (\mathbf{A1.17})$$

  - ▪ Melt inclusion (R_i) and host (R_h) radius: Set to measured radii.
- o The volume change $\left(1 + \frac{\Delta V_i}{V_{i0}}\right)$ is multiplied by the *initial* volume (V_i). The newly calculated volume describes the initial volume of the melt inclusion accounting for elastic deformation. In step 2, this volume is compared with the *intermediate* volume (V_{int}), if the *intermediate* volume is smaller, bubble growth is predicted.

Intermediate volume calculation

Step 1. Calculate partial molar volumes.
  Partial molar volumes for each melt component are calculated using the approach used in the first *initial* volume calculation. However, the following parameters are different.
- Temperature is set to the CO_2 closure temperature.
  - o The Dodson equation is used to determine closure temperature (Dodson, 1973).
  - o CO_2 diffusivity is calculated using eq. 30 of Zhang et al. (2007).
  - o The diffusive length scale is set to the radius of the melt inclusion.
  - o The cooling rate is input by the user.

- o MIMiC can calculate either the cooling rate or diffusive length scale if one of these parameters is unknown (see Appendix 2).
- Pressure is set to the *intermediate* pressure (P_{int}), which is calculated with Newman and Lowenstern (2002). This calculation involves several parameters.
  - o Melt H_2O contents: Set to the measured contents.
  - o Melt CO_2 contents: Set to the measured contents. It should be noted that if the measured CO_2 contents are reported as 0 ppm, the model predicts negligible CO_2 exists in the vapor bubble. This is because a CO_2 bearing vapor cannot coexist with a CO_2-free melt, if equilibrium is assumed.
  - o Temperature: Set to the CO_2 closure temperature.

Step 2. Calculate volume.

The volume of the melt in the *intermediate* state ($V_{int,melt}$) is calculated using the approach used in the first *initial* volume calculation.

- Instead of using the PEC/PEM corrected melt inclusion composition, the measured melt inclusion composition is used in Eq. A1.8.
  - o The mass of the intermediate melt is 100 g minus the mass of PEC olivine (in g), or plus the mass of PEM olivine (in g).
- Partial molar volumes from step 1 are used in the volume calculation (Eq. A1.9).

Step 3. Recalculate volume.

The volume of the melt inclusion is calculated based on whether PEC/PEM occurred.

- If PEM occurred, the volume of the intermediate melt inclusion is the volume of the intermediate melt.
- If PEC occurred, the volume of the intermediate melt inclusion (V_{int}) includes the volume of PEC olivine (V_{PEColv}), see Eq. A1.18. V_{PEColv} is calculated using Eqs. A1.11-A1.13. The olivine of interest has an Fo intermediate between the host olivine Fo (Fo_{host}) and the olivine Fo in equilibrium with the *intermediate* state melt inclusion (Fo_{int}). The pressure terms are set to P_{int}, and the temperature terms are set to T_{int}.

$$V_{int} = V_{int,melt} + \frac{M_{olv}}{\rho_{olv}} \qquad (\mathbf{A1.18})$$

The volume of the melt inclusion is recalculated based on whether or not PEC/PEM occurred.

- If PEC occurred, V_{int} must be increased by an amount appropriate for the mass of olivine crystallized (*wt% PEC*), which can be done using Eq. A1.12 and substituting *wt% PEC* for *wt% PEM*.
- If PEM occurred, no correction is necessary.

Iterative initial volume calculation

If the *initial* volume of the melt inclusion (accounting for thermal expansion and elastic deformation of the host) is greater than the *intermediate* volume of the melt inclusion, bubble growth is predicted to have occurred. The vapor bubble volume is determined by iteratively guessing the vapor bubble volume (V_{VB}) and recalculating the *initial* volume using bubble-growth-corrected parameters (Fig. A1.1). For each iteration, the volume of the vapor bubble is guessed

using the method described below. The mass of CO_2 in the vapor bubble is determined (Eq. A1.4), and that CO_2 is added into the glass composition by mass balance (Eq. A1.6). Steps 1.1-1.3 are followed to determine the V_i. Elastic deformation of the host is calculated (Eq. 1.15). A solution is attained if Vi is within 0.001% of the sum of V_{VB} and V_{int}. If a solution is not reached, the guess of V_{VB} is adjusted and the calculation is performed again.
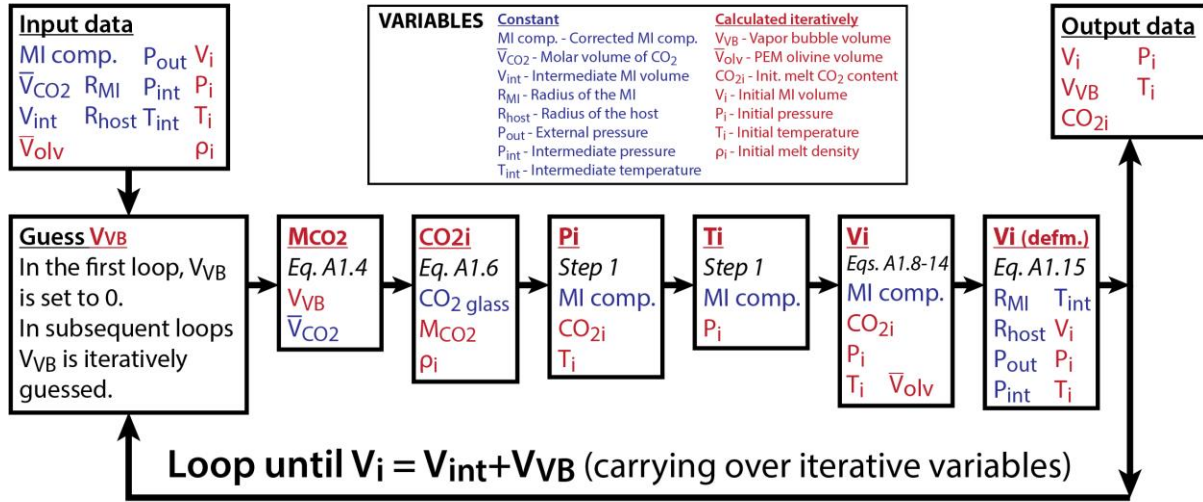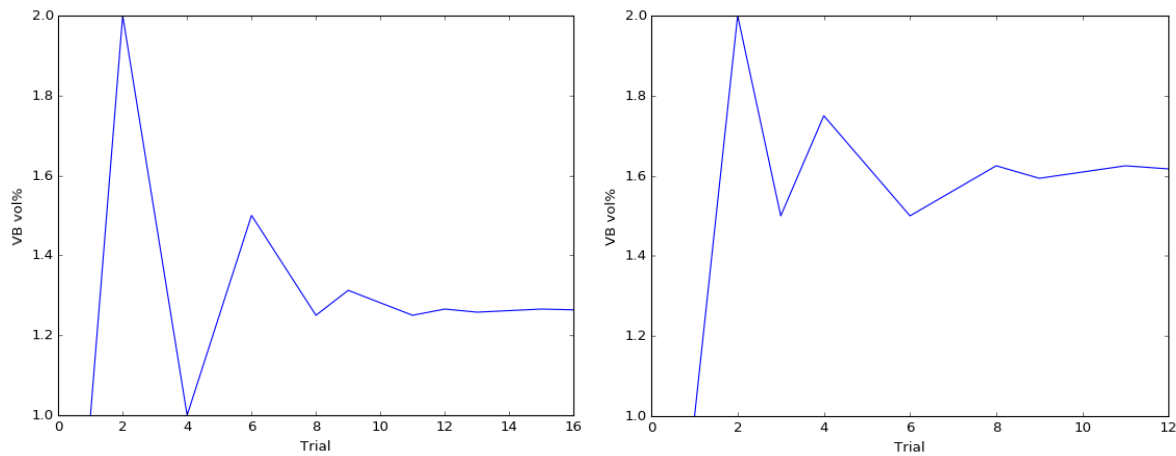

Figure A1.1. Iterative method for performing the vapor bubble correction.

The iterative method for guessing V_{VB} starts with a guess of 0 vol%. The volume is increased by increments of 1 vol% until $V_i < (V_{int} + V_{VB})$. When that occurs, the increment is halved, and the vol% increment changes signs (i.e., the increment is subtracted). This continues until the next change in the V_i to $(V_{int} + V_{VB})$ relationship occurs. Then, the increment is halved, and the sign changed again. This continues until Vi is within 0.001 vol% of $V_{int} + V_{VB}$. See Fig. A1.2 for examples of this calculation on melt inclusions from Seguam and Fuego. A solution is typically attained in 10-20 iterations.

Figure A1.2. Examples of the iterative method of bubble calculation. Note the increase in 1 vol% for the first few guesses until the bubble volume is overshot. Then, the vol% increment changes to 0.5, 0.25, etc. A solution is typically reached after 10-20 iterations.

<u>Model assumptions</u>

1. We consider elastic deformation of the host, but we do not consider the effect of plastic deformation. This is a simplification because cyclical heating stage experiments show evidence of plastic deformation (Sobolev and Danyushevsky, 1994; Massare et al., 2002; Schiavi et al., 2016), and models predict the effect (Tait, 1992; Zhang, 1998). However, because the greatest overpressures (i.e., difference in pressure of the melt inclusion versus that of the external environment) exist over short timescales upon eruption and other modeled processes act to decrease this overpressure (e.g., cooling, elastic deformation), we assume this effect is negligible.
2. We assume the thermal expansion coefficient of olivine does not vary with temperature.
3. We assume that diffusive loss of H^+ does not have an effect on bubble growth.

In general, the assumptions listed above lead to underestimates of CO_2 contents. Therefore, CO_2 contents restored using this method are a minimum.

A1.2. Experimental rehomogenization

We have developed a technique to experimentally rehomogenize melt inclusions. Our approach is similar to that of Mironov et al. (2015), with a few key differences. Instead of an internally heated pressure vessel, we use a piston cylinder apparatus. This makes the technique more accessible because piston cylinders are a relatively common experimental apparatus. In place of a silicate melt matrix, we use KBr.

A major innovation of Mironov et al. (2015) was to add water to the matrix melt. Matrix water reduces the chemical gradient of H_2O between the melt inclusion and exterior environment, which leads to less diffusive loss of H^+ from melt inclusions with high water contents and promotes diffusive uptake of H^+ in melt inclusions with low water contents. This is important because diffusive loss of H^+ from melt inclusions may lead to a decrease in the internal pressure (Bucholz et al., 2013). It should be noted that the activity of H_2O in a KBr brine is likely different than that of a silicate melt. Therefore, a gradient in the chemical potential likely exists. However, we do not find that our melt inclusions underwent significant gain or loss of water during experiments, lending credence to our approach.

KBr was selected as the matrix material because it is a compliant material that deforms around olivine grains when raising the experiments up to pressure, reducing the potential for cracks to form in the olivines, and KBr is water soluble, making grain retrieval a simple process without the risk of damaging grains. Given short experiment duration (< 2 hours), chemical interaction between the KBr and the melt inclusions is unlikely unless decrepitation occurs. We analyzed three melt inclusions that appeared to have decrepitated to test for a chemical signature of the such interaction, and we found extreme enrichments of K_2O in those melt inclusions (Table 4), indicating decrepitation is easily identifiable.

<u>Method</u>

Sample preparation

The build of our experimental charge is demonstrated in Fig. A1.3. The sample capsule is constructed from 0.18-inch Pt tubing. To construct the capsule, one end of the Pt tubing is crimped using a drill chuck. The crimped ends are then welded shut. The tube is then cut to length (appropriate for a 1/4" Al_2O_3 ceramic sleeve, but with excess material to create a mechanically sealed lid), and the bottom is flattened. The sample is then loaded into the capsule. First, brucite is added in the appropriate quantity to set the bulk H_2O contents (silicate, KBr, and olivines) of the experiment to the desired value. Then, KBr and olivines are added incrementally, allowing for KBr to separate olivine grains from one another, the brucite, and the open end of the capsule. A Pt lid for the capsule is cut to fit the inner diameter of the tube. Excess tubing is then folded over the lid in order to form a mechanical seal, which will completely set when the charge is brought up to experimental pressure (this occurs before heating). The Pt capsule is then loaded into the assembly shown in Fig.A1.3.
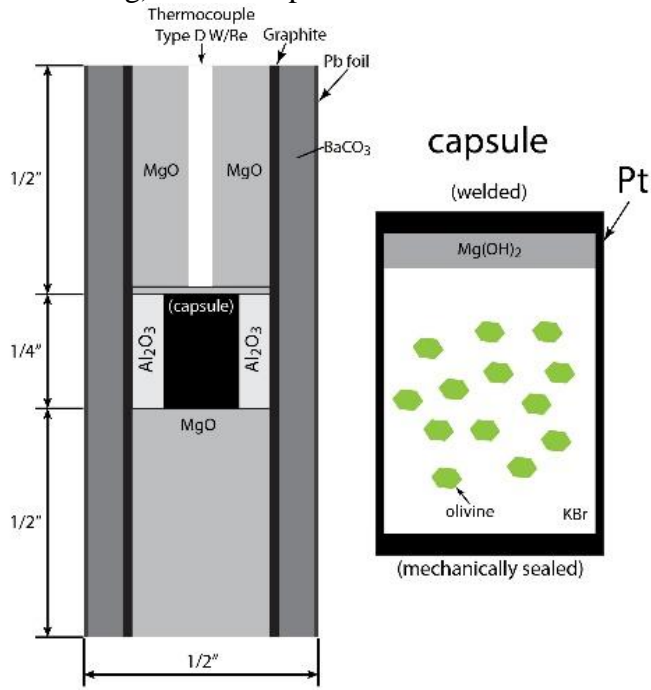

Figure A1.3. Diagram of experimental charge.

Running experiment

Samples are brought up to the desired experimental pressure (500-800 MPa) slowly (<10 MPa/s). Samples are then heated in a stepwise manner in order to avoid failures. First, samples are heated to 200 °C for 10 minutes. Load pressure gradually decreases and needs to be increased. Next, samples are heated to 400 °C for 30 minutes. Pressure is checked, and raised back to the set point if necessary, periodically during this time. Samples are then raised to the experimental temperature and held at this temperature for up to 2 hours. The duration of the experiment should be adjusted to minimize this time, while ensuring complete homogenization of melt inclusions. Samples are quenched at a rate of ~70 °C/s (Zhang and Behrens, 2000).

Sample retrieval

The Pt casule is sliced open using a razor, and the entire capsule is then submerged in warm tap water in a petri dish. Within a few minutes, the KBr fully dissolves in the water, and olivines fall out of the capsule into the dish.

A1.3. Raman spectroscopy reconstruction

In the Raman approach, the density of CO_2 in the vapor bubble is measured by Raman spectroscopy, and that CO_2 is added to the composition of the glass by mass balance. We review the Raman approach used by Rasmussen et al. (2018), which is similar to the methods used by other studies (e.g., Moore et al., 2015; Moore et al., 2018).

<u>Method</u>

Raman measurements

Measurements with the Raman spectrometer are performed on vapor bubbles in melt inclusions that are close to the surface ($<200\,\mu m$) but not intersected. For spectra containing a Fermi diad, the splitting is measured using a peak-fitting routine. Rasmussen et al. (2018) fit peaks with gaussian functions. The CO_2 density is calculated using a Raman densimeter appropriate for the instrumentation and analytical set-up (e.g., Fall et al., 2011; Lamadrid et al., 2017).

Calculation of CO_2 mass

The volume of the vapor bubble (V_{VB}) is measured. This is done using the same approaches outlined in the observed volume equation of state approach (see section 1.1). The mass of CO_2 (M_{CO2}) in the bubble is calculated using the measured density and the observed volume of the vapor bubble.

Melt inclusion mass

Melt inclusion volume is measured in the same way as vapor bubble volume. If measurements are performed petrographically, the melt inclusion is assumed to be ellipsoidal. The third dimension of the melt inclusion (not visible petrographically) is typically assumed to be equivalent to the short-measured dimension (this is because a common strategy for mounting melt inclusions is to put the shortest dimension normal to the cross-sectional plane in order to maximize the measurable area). Alternatively, the thickness of the melt inclusion can be measured by focusing to the top and bottom of the inclusion using a calibrated stage. In practice, this is very difficult because many melt inclusions have smooth interfaces that don't come into sharp focus. Chemical analyses of melt inclusion volatile and major elements are conducted. The density of the melt inclusion is determined using the measured composition and partial molar volumes (e.g., Lesher and Spera, 2015) of each chemical component . The mass of the melt inclusion is calculated using the density (ρ_{MI}) and volume (V_{MI}) of the melt inclusion.

Reconstruct CO_2

The restored CO_2 content ($CO_{2\ restored}$) is calculated by adding the mass of CO_2 in the vapor bubble to the mass of CO_2 in the melt inclusion ($CO_{2\ glass}$) by mass balance (Eq. A1.6).

A1.4. References

Abramson, E.H., Brown, J.M., Slutsky, L.J. and Zaug, J., 1997. The elastic constants of San Carlos olivine to 17 GPa. 102(B6): 12253-12263.

Anderson, A.T. and Brown, G.G., 1993. CO2 contents and formation pressures of some Kilauean melt inclusions. American Mineralogist, 78(7-8): 794-803.

Aster, E.M., Wallace, P.J., Moore, L.R., Watkins, J., Gazel, E. and Bodnar, R.J., 2016. Reconstructing CO2 concentrations in basaltic melt inclusions using Raman analysis of vapor bubbles. Journal of Volcanology and Geothermal Research, 323: 148-162.

Bucholz, C.E., Gaetani, G.A., Behn, M.D. and Shimizu, N., 2013. Post-entrapment modification of volatiles and oxygen fugacity in olivine-hosted melt inclusions. Earth and Planetary Science Letters, 374: 145-155.

Colman, A., Sinton, J.M. and Wanless, V.D., 2015. Constraints from melt inclusions on depths of magma residence at intermediate magma supply along the Galápagos Spreading Center. Earth and Planetary Science Letters, 412: 122-131.

Dodson, M.H., 1973. Closure temperature in cooling geochronological and petrological systems. Contr. Mineral. and Petrol., 40(3): 259-274.

Duan, Z. and Zhang, Z., 2006. Equation of state of the H2O, CO2, and H2O–CO2 systems up to 10 GPa and 2573.15K: Molecular dynamics simulations with ab initio potential surface. Geochimica et Cosmochimica Acta, 70(9): 2311-2324.

Fall, A., Tattitch, B. and Bodnar, R.J., 2011. Combined microthermometric and Raman spectroscopic technique to determine the salinity of H2O–CO2–NaCl fluid inclusions based on clathrate melting. Geochimica et Cosmochimica Acta, 75(4): 951-964.

Giordano, D., Russell, J.K. and Dingwell, D.B., 2008. Viscosity of magmatic liquids: a model. Earth and Planetary Science Letters, 271(1-4): 123-134.

Hacker, B.R., Abers, G.A. and Peacock, S.M., 2003. Subduction factory 1. Theoretical mineralogy, densities, seismic wave speeds, and H2O contents. Journal of Geophysical Research: Solid Earth, 108(B1).

Hauri, E.H., Maclennan, J., McKenzie, D., Gronvold, K., Oskarsson, N. and Shimizu, N., 2018. CO2 content beneath northern Iceland and the variability of mantle carbon. Geology, 46(1): 55-58.

Lamadrid, H.M., Moore, L.R., Moncada, D., Rimstidt, J.D., Burruss, R.C. and Bodnar, R.J., 2017. Reassessment of the Raman CO2 densimeter. Chemical Geology, 450: 210-222.

Lange, R.A., 1997. A revised model for the density and thermal expansivity of K 2 O-Na 2 O-CaO-MgO-Al 2 O 3-SiO 2 liquids from 700 to 1900 K: extension to crustal magmatic temperatures. Contr. Mineral. and Petrol., 130(1): 1-11.

Lange, R.A. and Carmichael, I.S., 1987. Densities of Na2O-K2O-CaO-MgO-FeO-Fe2O3-Al2O3-TiO2-SiO2 liquids: new measurements and derived partial molar properties. Geochimica et Cosmochimica Acta, 51(11): 2931-2946.

Lesher, C.E. and Spera, F.J., 2015. Thermodynamic and transport properties of silicate melts and magma, The Encyclopedia of Volcanoes (Second Edition). Elsevier, pp. 113-141.

Liu, W., Kung, J. and Li, B., 2005a. Elasticity of San Carlos olivine to 8 GPa and 1073 K. Geophysical Research Letters, 32(16).

Liu, W. and Li, B., 2006. Thermal equation of state of (Mg0.9Fe0.1)2SiO4 olivine. Physics of the Earth and Planetary Interiors, 157(3): 188-195.

Liu, Y., Zhang, Y. and Behrens, H., 2005b. Solubility of H2O in rhyolitic melts at low pressures and a new empirical model for mixed H2O–CO2 solubility in rhyolitic melts. Journal of Volcanology and Geothermal Research, 143(1-3): 219-235.

Lloyd, A.S., Plank, T., Ruprecht, P., Hauri, E.H. and Rose, W., 2013. Volatile loss from melt inclusions in pyroclasts of differing sizes. Contr. Mineral. and Petrol., 165(1): 129-153.

Maclennan, J., 2017. Bubble formation and decrepitation control the CO2 content of olivine-hosted melt inclusions. Geochemistry, Geophysics, Geosystems, 18(2): 597-616.

Massare, D., Métrich, N. and Clocchiatti, R.J.C.G., 2002. High-temperature experiments on silicate melt inclusions in olivine at 1 atm: inference on temperatures of homogenization and H2O concentrations. 183(1-4): 87-98.

Mironov, N., Portnyagin, M., Botcharnikov, R., Gurenko, A., Hoernle, K. and Holtz, F., 2015. Quantification of the CO2 budget and H2O–CO2 systematics in subduction-zone magmas through the experimental hydration of melt inclusions in olivine at high H2O pressure. Earth and Planetary Science Letters, 425: 1-11.

Montierth, C., Johnston, A.D. and Cashman, K.V., 1995. An empirical glass-composition-based geothermometer for Mauna Loa lavas. Mauna Loa Revealed: Structure, Composition, History, and Hazards: 207-217.

Moore, L.R., Gazel, E., Tuohy, R., Lloyd, A.S., Esposito, R., Steele-MacInnis, M., Hauri, E.H., Wallace, P.J., Plank, T. and Bodnar, R.J., 2015. Bubbles matter: An assessment of the contribution of vapor bubbles to melt inclusion volatile budgets. American Mineralogist, 100(4): 806-823.

Moore, L.R., Mironov, N., Portnyagin, M., Gazel, E. and Bodnar, R.J., 2018. Volatile contents of primitive bubble-bearing melt inclusions from Klyuchevskoy volcano, Kamchatka: Comparison of volatile contents determined by mass-balance versus experimental homogenization. Journal of Volcanology and Geothermal Research, 358: 124-131.

Newman, S. and Lowenstern, J.B., 2002. VolatileCalc: a silicate melt–H2O–CO2 solution model written in Visual Basic for excel. Computers & Geosciences, 28(5): 597-604.

Ochs, F.A. and Lange, R.A., 1999. The density of hydrous magmatic liquids. Science, 283(5406): 1314-1317.

Pamukcu, A.S., Gualda, G.A., Bégué, F. and Gravley, D.M., 2015. Melt inclusion shapes: Timekeepers of short-lived giant magma bodies. Geology, 43(11): 947-950.

Putirka, K.D., Perfit, M., Ryerson, F.J. and Jackson, M.G., 2007. Ambient and excess mantle temperatures, olivine thermometry, and active vs. passive upwelling. Chemical Geology, 241(3–4): 177-206.

Rasmussen, D.J., Plank, T.A., Roman, D.C., Power, J.A., Bodnar, R.J. and Hauri, E.H., 2018. When does eruption run-up begin? Multidisciplinary insight from the 1999 eruption of Shishaldin volcano. Earth and Planetary Science Letters, 486: 1-14.

Riker, J., 2005. The 1859 Eruption of Mauna Loa Volcano, Hawai'i: Controls on the Development of Long Lava Channels, University of Oregon.

Schiavi, F., Provost, A., Schiano, P. and Cluzel, N., 2016. P–V–T–X evolution of olivine-hosted melt inclusions during high-temperature homogenization treatment. Geochimica et Cosmochimica Acta, 172: 1-21.

Shaw, A.M., Behn, M.D., Humphris, S.E., Sohn, R.A. and Gregg, P.M., 2010. Deep pooling of low degree melts and volatile fluxes at the 85 E segment of the Gakkel Ridge: Evidence from olivine-hosted melt inclusions and glasses. Earth and Planetary Science Letters, 289(3): 311-322.

Sides, I., Edmonds, M., Maclennan, J., Houghton, B.F., Swanson, D.A. and Steele-MacInnis, M.J., 2014. Magma mixing and high fountaining during the 1959 Kīlauea Iki eruption, Hawai'i. Earth and Planetary Science Letters, 400: 102-112.

Sobolev, A.V. and Danyushevsky, L.V., 1994. Petrology and geochemistry of boninites from the north termination of the Tonga Trench: constraints on the generation conditions of primary high-Ca boninite magmas. Journal of Petrology, 35(5): 1183-1211.

Steele-Macinnis, M., Esposito, R. and Bodnar, R.J., 2011. Thermodynamic model for the effect of post-entrapment crystallization on the H_2O–CO_2 systematics of vapor-saturated, silicate melt inclusions. Journal of Petrology, 52(12): 2461-2482.

Tait, S., 1992. Selective preservation of melt inclusions in igneous phenocrysts. American Mineralogist, 77(1-2): 146-155.

Toplis, M.J., 2005. The thermodynamics of iron and magnesium partitioning between olivine and liquid: criteria for assessing and predicting equilibrium in natural and experimental systems. Contr. Mineral. and Petrol., 149(1): 22-39.

Wallace, P.J., Kamenetsky, V.S. and Cervantes, P., 2015. Melt inclusion CO_2 contents, pressures of olivine crystallization, and the problem of shrinkage bubbles. American Mineralogist, 100(4): 787-794.

Wanless, V., Behn, M., Shaw, A. and Plank, T., 2014. Variations in melting dynamics and mantle compositions along the Eastern Volcanic Zone of the Gakkel Ridge: insights from olivine-hosted melt inclusions. Contr. Mineral. and Petrol., 167(5): 1005.

Xu, Z. and Zhang, Y., 2002. Quench rates in air, water, and liquid nitrogen, and inference of temperature in volcanic eruption columns. Earth and Planetary Science Letters, 200(3-4): 315-330.

Zhang, Y., 1998. Mechanical and phase equilibria in inclusion–host systems. Earth and Planetary Science Letters, 157(3): 209-222.

Zhang, Y. and Behrens, H., 2000. H_2O diffusion in rhyolitic melts and glasses. Chemical Geology, 169(1): 243-262.

Zhang, Y., Xu, Z., Zhu, M. and Wang, H., 2007. Silicate melt properties and volcanic eruptions. Reviews of Geophysics, 45(4).